Cronfa - Swansea University Open Access Repository

Paper:

Lee, H., Wu, J., Barbe, J., Jain, S., Wood, S., Speller, E., Li, Z., Castro, F., Durrant, J. et. al. (2017). Organic photovoltaic cell – a promising indoor light harvester for self-sustainable electronics. *Journal of Materials Chemistry A*
http://dx.doi.org/10.1039/C7TA10875C

Journal of
Materials Chemistry A

Accepted Manuscript

Journal of
Materials Chemistry A

Materials for energy and sustainability
www.rsc.org/MaterialsA

Volume 4 | Number 1 | 7 January 2016 | Pages 1–330

ISSN 2050-7488

ROYAL SOCIETY OF CHEMISTRY

175 YEARS

PAPER
Kun Chang, Zhaorong Chang et al.
Bubble-template-assisted synthesis of hollow fullerene-like
MoS₂ nanocages as a lithium ion battery anode material

This is an Accepted Manuscript, which has been through the Royal Society of Chemistry peer review process and has been accepted for publication.

Accepted Manuscripts are published online shortly after acceptance, before technical editing, formatting and proof reading. Using this free service, authors can make their results available to the community, in citable form, before we publish the edited article. We will replace this Accepted Manuscript with the edited and formatted Advance Article as soon as it is available.

You can find more information about Accepted Manuscripts in the author guidelines.

ROYAL SOCIETY
OF CHEMISTRY

rsc.li/materials-a

Organic photovoltaic cell – a promising indoor light harvester for self-sustainable electronics

*Harrison Ka Hin Lee,[a] Jiaying Wu,[b] Jérémy Barbé,[a] Sagar M. Jain,[a] Sebastian Wood,[c] Emily M. Speller,[a] Zhe Li,[a] Fernando A. Castro,[c] James R. Durrant,[ab] and Wing Chung Tsoi[*a]*

[*]Email: w.c.tsoi@swansea.ac.uk

[a]SPECIFIC, College of Engineering, Bay Campus, Swansea University, Swansea, SA1 8EN, UK

[b]Department of Chemistry and Centre for Plastic Electronics, Imperial College London, London, SW7 2AZ, UK

[c]National Physical Laboratory, Hampton Road, Teddington, TW11 0LW, UK

[†]Electronic supplementary information (ESI) available.

Journal of Materials Chemistry A Accepted Manuscript

Abstract

Photovoltaic cells are attracting significant interest for harvesting indoor light for low power consumption wireless electronics such as those required for smart homes and offices, and the rapidly-growing Internet of Things. Here, we explore the potential of solution processable, small molecule photovoltaic cells as indoor power sources. By optimizing solvent vapour annealing (SVA) time to the photovoltaic layer, a balance between its crystallization and phase separation is obtained, resulting in a record power conversion efficiency of over 28 % under fluorescent lamps of 1000 lux, generating a maximum power density of 78.2 $\mu W/cm^2$ (>10 % efficiency under AM1.5G). This high indoor performance surpasses silicon based photovoltaic cells, and is similar to gallium arsenide photovoltaic cells. Besides, the ratios of the voltage at maximum power point to the open circuit voltage are similar from indoor lighting to one sun condition, which is unique and allows a less power consuming method to track the maximum power point for a broad range of light intensities (potentially attractive for wearable PV). New insight on the effect of SVA to the indoor and one sun performance is provided by advanced optoelectronic characterization techniques, which shows that the mobility-lifetime products as a function of charge carrier density can be correlated well to the performance at different light levels. Our results suggest that organic photovoltaic cell could be promising as indoor power source for self-sustainable electronics.

1. Introduction

Organic photovoltaic (OPV) cells using solution processable small molecule donors have been receiving more attention in recent years due to the following unique features over polymer donors.[1] Unlike polymers which have a batch-to-batch variation in molecular weight distribution during synthesis which can lead to poor device reproducibility,[2] small molecules have a well-defined structure and thus a monodisperse molecular weight which allows easier purification and better reproducibility.[1] Moreover, the power conversion efficiency (PCE) of such cells can now exceed 11 %,[3,4] approaching the highest PCE's (over 13 %)

Although the main market of PV is for outdoors, the potential of PV, especially low-cost PV, for harvesting energy from indoor light is becoming very attractive because of the rapid growth in potential applications, including local powering of low power consumption electronic devices, and charging batteries. One of the exciting opportunities is to harvest indoor light to provide power for electronics used for Internet of Things (IoT) with wireless internet connection, which the industry forecasts tens of billion devices will be connected by 2020. IoT allows communication between small electronic devices via networks, in which wireless electronic devices (containing sensors, actuators, etc.) are one of the key components and can lead to next generation smart home/office, retail sector, and manufacturing line. For these devices, with typically low power consumption (up to milliwatts), harvesting sufficient energy from the indoor ambient environment is a key challenge for wireless devices with unattended operation for months or ideally years. It has been suggested that harvesting ambient light using PV devices installed indoors is a particularly attractive solution to deal with this challenge. Here, we discover a solution

3

processable, small molecule photovoltaic cell with record high indoor performance among

organic photovoltaic cells, and significantly better than silicon based photovoltaic cells.

Furthermore, we find that advanced optoelectronic characterization techniques can provide

new insight to understand the device physics under low light levels (versus 1 sun).

Different types of PV devices including silicon, III–V semiconductors, dye-sensitized,

organic and perovskite PV cells have been studied under indoor lighting conditions,[5–12] with

some of them showing promising indoor performance.[8,10,11] Among them, a wide bandgap

III–V semiconductor PV, GaInP, has demonstrated the highest performance to date, with an

open-circuit voltage (V_{OC}) approaching 1.2 V, generating 92.7 $\mu W/cm^2$ under 1000 lux

fluorescent lamps.[8] There have been some studies of OPV devices for indoor applications.

Steim et al. showed that the shunt resistance, R_{Sh}, is more critical than series resistance, R_S,

to the performance under low light conditions and suggested that a minimum R_{Sh} of 85

$k\Omega cm^2$ is required for low light level applications.[13] Later, Lechêne et al. further explored

how R_{Sh} and the reverse saturated current, J_0, affect the low light performance and

concluded that the absolute value of R_{Sh} required varies for different systems depending on

the ratio of J_0 to short-circuit current density (J_{SC}). There are also some demonstrations

using OPV for indoor applications including charging a super-capacitor and powering

wireless sensor nodes.[14,15] Recently, OPV devices with respectable one sun performance

have been shown to yield more than 22% PCE when tested under LEDs illumination.[16]

However, despite these advances, the indoor performance of PV devices is still far from the

theoretical limit of 50 % PCE for fluorescent lamps and ca. 60 % PCE for LEDs lighting.[17]

Recently, a promising OPV system has emerged using solution processable blends of

small molecule donor and fullerene acceptor, namely benzodithiophene terthiophene

rhodamine:[6,6]-phenyl-C$_{71}$-butyric acid methyl ester (BTR:PC$_{71}$BM), molecular structure of

BTR is available in Fig. S1†, showing attractive performance under one sun, with optimum

active layer thickness at 250 nm with fill factors (*FF*) up to 77 % and PCE of 9.3 %. The active

layer thickness can be further increased to 400 nm without a significant drop in efficiency,

attributed to significantly suppressed bimolecular recombination.[18–20] More importantly, it

has a high external quantum efficiency (EQE) across the visible spectrum and a high V_{OC}

under one sun, both essential requirements for efficient indoor PV device

performance.[18,21,22] Therefore, we envision that it is a potentially promising material system

for indoor PV application, as evaluated in the study reported herein.

The system BTR:PC$_{71}$BM, like other small molecule:fullerene systems, requires

additional processing treatment to obtain its best device performance.[1] In this case, solvent

vapour annealing (SVA) of the blend films is the additional step used to achieve high

efficiency.[18,23] Engmann et al. have demonstrated the importance of choosing the correct

solvent for SVA: a solvent in which the active material is moderately soluble, such as

tetrahydrofuran (THF), is more suitable for optimizing device performance than a good

solubility solvent, such as chloroform.[23] Although several studies have looked at the

morphological changes of BTR:PC$_{71}$BM films with and without SVA, the influence of SVA on

the optoelectronic properties of the devices is still unclear.

In this work, we study the effect of the SVA time (using THF) on the BTR:PC$_{71}$BM

layer and the resulting device performance under one sun and indoor lighting conditions,

from 100 lux to 2000 lux which include most of the indoor environments.[24,25] We find that

the optimised BTR:PC$_{71}$BM cell can achieve an outstanding PCE of over 28 % under indoor

lighting (together with an attractive PCE under solar illumination). Additionally, the V_{max} to

5

V_{OC} ratio is stable from low light to high light levels, which is beneficial as it simplifies the

tracking of maximum power point. Furthermore, SVA has a significantly weaker effect on

the *PCE* of the devices under 1000 lux illumination than that under one sun. The effect of

SVA time on the performance of the devices is correlated to the film morphology of the

BTR:PC_{71}BM studied by ultraviolet-visible (UV-Vis) absorption, grazing incidence x-ray

diffraction (GIXRD), atomic force microscopy (AFM), and photoluminescence (PL).

Furthermore, optoelectronic characterization including photocurrent, charge extraction (CE),

and transient photovoltage (TPV) measurements over a range of light levels provide

significant insight into the effect of SVA time on the device performance, particularly the

difference between indoor lighting and one sun conditions.

2. Experimental

2.1 Materials

BTR and $PC_{71}BM$ were purchased from 1-Material and Solenne BV, respectively. Chloroform (CF) and anhydrous tetrahydrofuran (THF) are purchased from Sigma-Aldrich. Poly(3,4-ethylenedioxythiophene)-poly(styrenesulfonate) (PEDOT:PSS), Clevios P VP AI 4083, was purchased from Heraeus. All materials were used as received without further purification.

2.2 Device fabrication and characterization

Indium tin oxide (ITO) glass substrates (15 $\Omega/\square$) were cleaned sequentially with detergent (Hellmanex), deionized water, acetone, and isopropyl alcohol in an ultrasonic bath. BTR and $PC_{71}BM$ (1:1 weight ratio) were dissolved in CF with a total concentration of 40 mg/ml on a 60 °C hotplate stirred overnight in a nitrogen filled glovebox. PEDOT:PSS was first spin-coated (4000 r.p.m. for 60 s) on plasma cleaned ITO glass substrates in air followed by 150 °C annealing on a hotplate for 10 minutes. After transferring the samples to the nitrogen filled glovebox, the blend solution was then spin-coated on the PEDOT:PSS coated substrates at an optimized speed of 1500 r.p.m. for 15 s resulted in ca 220 nm active layer thickness measured by a profilometer. SVA treatment was performed in a sectioned petri dish. THF of 1 ml was put in a section of the petri dish to ensure similar surface area exposed to the solvent vapour environment. The THF filled petri dish was covered with a lid for at least 2 minutes before doing the SVA treatment to the active layer. The samples were placed in the other sections of the petri dish with the active layer facing up for different exposure times as specified in the main text. Finally, 30 nm of calcium and 100 nm of aluminium were thermally evaporated onto the active layer in an evaporator at a based pressure of 2×10^{-5} mbar, forming devices with active area of 0.15 cm^2. All devices were

7

encapsulated with glass slides with the aid of UV-epoxy before measurements. *J-V*

characterizations were performed by a Keithley 2400 sourcemeter under both solar

simulator (Newport 92193A-1000) with intensity of ca 90 mW/cm^2 and fluorescent lamps

(Osram L18W/827). The lux levels of the fluorescence lamps were measured by a luxmeter,

(LX-1330B). The intensity calibration was mentioned in a previous work.[21] EQE spectra were

obtained by QEX10 Quantum Efficiency Measurement System.

2.3 Characterization

The UV-Vis absorbance spectra were measured in the range 200 – 1000 nm using a Perkin

Elmer Lambda 750 spectrophotometer. BTR:PC$_{71}$BM blend films with and without SVA

treatment were prepared directly on quartz and a quartz substrate was used as a reference

sample for calibration. GIXRD measurements were carried out using a Bruker D8 Discover

instrument with a CuKα beam (wavelength is 0.15418 nm) at 40 kV and 40 mA, scan

parameters of 0.1 s/step at 0.01° of 2θ step size. A FluoroMax-4 spectrofluorometer (Horiba

Scientific) was used to measure the photoluminescence spectra of BTR:PC$_{71}$BM blend films

on quartz in the range 560 – 1000 nm using an excitation wavelength of 532 nm. The

integration time was 0.2 s. The entrance and exit slits were 5 nm. Diffraction gratings with

1200 gr/mm were used for the excitation and emission monochromators. The spectrum of

the lamp was measured by a photodiode located between the sample and the excitation

monochromator, and corrected by a calibration file (R1c: corrected lamp spectrum). The

emission spectrum S1 were corrected by a calibration file (S1c: corrected emission spectrum)

and further divided by the corrected reference signal R1c. The data in the manuscript show

the S1c/R1c signal. AFM was performed with an AIST-NT CombiScope in non-contact mode

using a Budget Sensors Multi75Al-G probe with tip radius < 10 nm. Surface height profiles

were levelled by fitting each line with a second order polynomial, before evaluating the root

mean square (RMS) roughness values. The corrected photocurrent $J_{ph}(V)$ was measured

from the difference in *J-V* response between the dark response $J_{dark}(V)$ and the light

response $J_{light}(V)$ by pulsed illumination to avoid overheating the samples. The pulsed

illumination was generated by a ring of 12 white LEDs with a fast-switching metal oxide field

effect transistor. The one sun equivalent illumination was calibrated by matching the value

of J_{SC} obtained under the AM1.5G illumination. The light was switched on for approximately

2 ms to allow the current reaching the steady state and a much longer time was used after

switching off the light to avoid the device to cool down. The potential bias was applied by a

Keithley 2400 sourcemeter, and the voltage across the device was measured by a Tektronix

TDS3032B Oscilloscope with a 1-MΩ input impedance. Charge extraction was used to

determine the average charge carrier densities in devices under different illumination levels

and under different biases (open circuit and short circuit conditions in this study). The

desired light intensity was provided by the ring of 12 white LEDs. The device was held at

open circuit under an initial bias with a background light level and then switched to short

circuit with the light off simultaneously. The voltage transient was acquired with a DAQ card

connected to a Tektronix TDS3032B Oscilloscope. The voltage transients were converted

into current transients through Ohms law. The total charges for the calculation of *n* was

extracted by integrating the current transients. For the TPV measurements, the device was

held at open circuit condition under different background light intensity controlled by the

ring of white LEDs. A small additional optical excitation provided by a pulsed Continuum

Minilite Nd:YAG laser at 532nm with a pulse width of < 10 nm was applied to the device

under measurement. This small excitation generated a small voltage decay transient which

was captured by an oscilloscope. The decay was fitted with a mono-exponential model to

obtain the small perturbation carrier lifetime and finally to be used to estimate the total

charge carrier lifetime within the device.

3. Results and discussion

3.1 Device performance under a solar simulator and fluorescent lamps
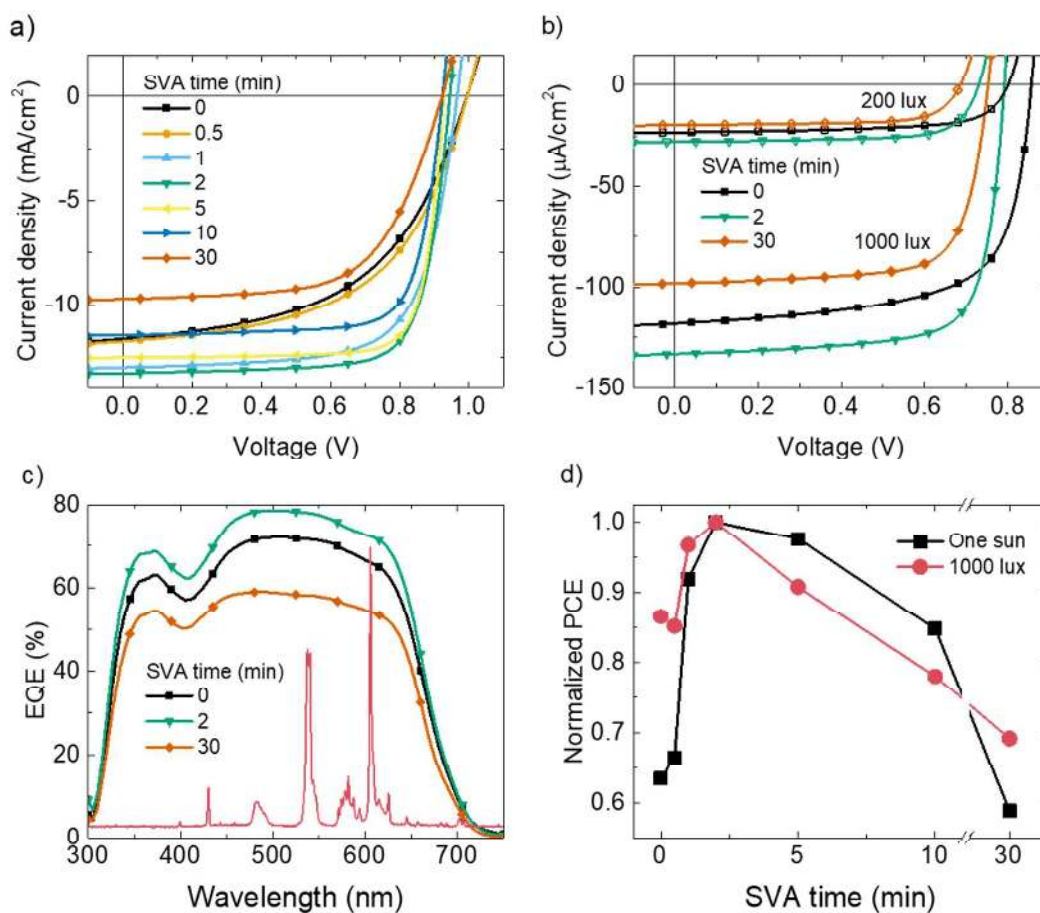

Fig. 1 *J-V* characterization for a series of different SVA times, measured under (a) one sun and (b) fluorescent lamps. (c) EQE spectra of the devices with 0 minutes, 2 minutes, and 30 minutes SVA time. Spectrum of the fluorescent lamps is also plotted (arbitrary scale). (d) Normalized PCE measured under one sun and 1000 lux fluorescent lamps for devices with different SVA times.

Table 1 Device parameters for different SVA times, measured under AM1.5G with 90 mW/cm^2 intensity. Values in the brackets are data obtained under 1000 lux fluorescent lamps.

SVA time (min)	J_{SC} (mA/cm^2) [μA/cm^2]	V_{OC} (V)	FF (%)	P_{max} (mW/cm^2) [μW/cm^2]	PCE (%)
0	11.6 [118.1]	0.994 [0.856]	51.6 [67.4]	5.97 [6.8]	6.6 [24.2]
0.5	11.8 [117.8]	0.995 [0.859]	53.5 [66.3]	6.26 [66.3]	7.0 [23.8]
1	13.0 [127.0]	0.966 [0.815]	68.9 [73.6]	8.65 [74.8]	9.6 [27.0]
2	**13.3 [133.1]**	**0.945 [0.791]**	**75.1 [75.2]**	**9.42 [78.2]**	**10.5 [28.1]**
5	12.5 [121.8]	0.928 [0.755]	79.1 [77.7]	9.19 [71.0]	10.2 [25.3]
10	11.5 [108.8]	0.923 [0.747]	75.4 [75.6]	7.98 [60.9]	8.9 [21.8]
30	9.7 [98.1]	0.922 [0.754]	61.9 [73.7]	5.54 [53.5]	6.2 [19.3]

The effect of active layer SVA time (from 0 minutes to 30 minutes) on the performance of BTR:PC$_{71}$BM cells was investigated under both AM1.5G and indoor lighting conditions. Fig. 1a shows the corresponding current density-voltage (*J-V*) characteristics of BTR:PC$_{71}$BM devices under AM1.5G and the device parameters are listed in Table 1. The variation of each device parameter with the SVA time is shown in Fig. S2†. V_{OC} of the devices with no SVA and 0.5 minutes SVA are the highest (approaching 1 V), and it decreases gradually with SVA time, saturating at about 0.92 V from 10 minutes SVA onward. The drop in V_{OC} could be correlated to the improved crystallinity (see section 2.2) of BTR in the blend films upon SVA, as improved crystallization could raise the highest occupied molecular orbital (HOMO) level of the donor,[26] and thus reduce the V_{OC}.[27] The J_{SC} and *FF* increase with SVA time until an optimum time, and then decrease. Moderate SVA times of 2 minutes and 5 minutes result in the highest J_{SC} and *FF* of 13.3 mA/cm^2 and 79.1 %, respectively. Overall, the PCE mainly follows the trend of the J_{SC} and *FF* with SVA time, with the efficiency peaking at 10.5 % (2 minutes SVA) under AM1.5G.

Next, we move to discuss devices tested under an array of fluorescent lamps which mimics a typical indoor environment. Fig. 1b shows the *J-V* curves of 0 minutes, 2 minutes,

and 30 minutes SVA obtained under 200 lux and 1000 lux. The device with 2 minutes SVA

shows the highest PCE of 26.2 % (200 lux) and 28.1 % (1000 lux), generating a maximum

power output density (P_{max}) of 14.6 μW/cm^2 and 78.2 μW/cm^2, respectively. The record high

performance can be explained based on our previous work.[21] Firstly, the bandgap of BTR is

about 1.8 eV corresponding to the absorption onset of ca. 700 nm (see Fig. 2a for the

absorbance spectra) which is the ideal energy gap to harvest indoor light such as fluorescent

lamps and visible light-emitting diodes.[17,28] This is further confirmed by Fig. 1c which shows

that the external quantum efficiency (EQE) spectra of the devices with 0 minutes, 2 minutes

and 30 minutes SVA overlap well with that of the fluorescent lamps (also shown in Fig. 1c)

and has a peak EQE of 78.6 % at 515 nm for the device treated with SVA for 2 minutes. Note

that the spectrum for the device after 30 minutes SVA shows the lowest EQE and the

spectrum for 0 minutes (no SVA) shows an intermediate EQE, consistent with the values of

the J_{SC}. Secondly, a high V_{OC} under one sun and high small diode ideality factor η (obtained

by measuring the V_{OC} as a function of light intensity), are both beneficial to low light

performance.[21] Even if devices behave like an ideal diode (η = 1), there is still an

unavoidable voltage drop of 0.15 V to 0.25 V when the light intensity is reduced from one

sun to indoor lighting condition, independent of the absolute magnitude of the

voltage.[8,9,14,21] The BTR:PC$_{71}$BM studied herein exhibits a relatively high V_{OC} under one sun

(up to 1 V), which minimizes the fraction of the voltage lost at low light intensity. In addition,

all the BTR:PC$_{71}$BM devices measured herein (independent of SVA time) have η values close

to the ideal (see Fig. S3† for each device parameters at different light intensity), further

enhancing the low light level voltage output.[29]

To compare the effect of SVA time on the device performance under AM1.5G and

1000 lux, PCE under AM1.5G and 1000 lux with different SVA times were normalized to the

peak PCE (at 2 minutes SVA), as shown in Fig. 1d. Interestingly, for short SVA time (0

minutes or 0.5 minutes), the PCE under one sun has only around 65 % of the peak efficiency

whereas the PCE under 1000 lux fluorescent lamps maintains 86 % of the peak efficiency. To

investigate this difference, device parameters under 1000 lux were compared to those

under one sun for different SVA times, as shown in Fig. S2†. From this Figure, it is apparent

that the FF is the main parameter which exhibits the most significant enhancement from

AM1.5G to 1000 lux (also less V_{OC} reduction as shown in Fig. S2b). In order to elucidate the

origins of the enhanced performance, and specifically enhanced, obtained under low level

irradiation, and why this enhancement is dependent upon SVA time, we further investigated

the films and devices in terms of their film morphology and optoelectronic properties in the

following sections.
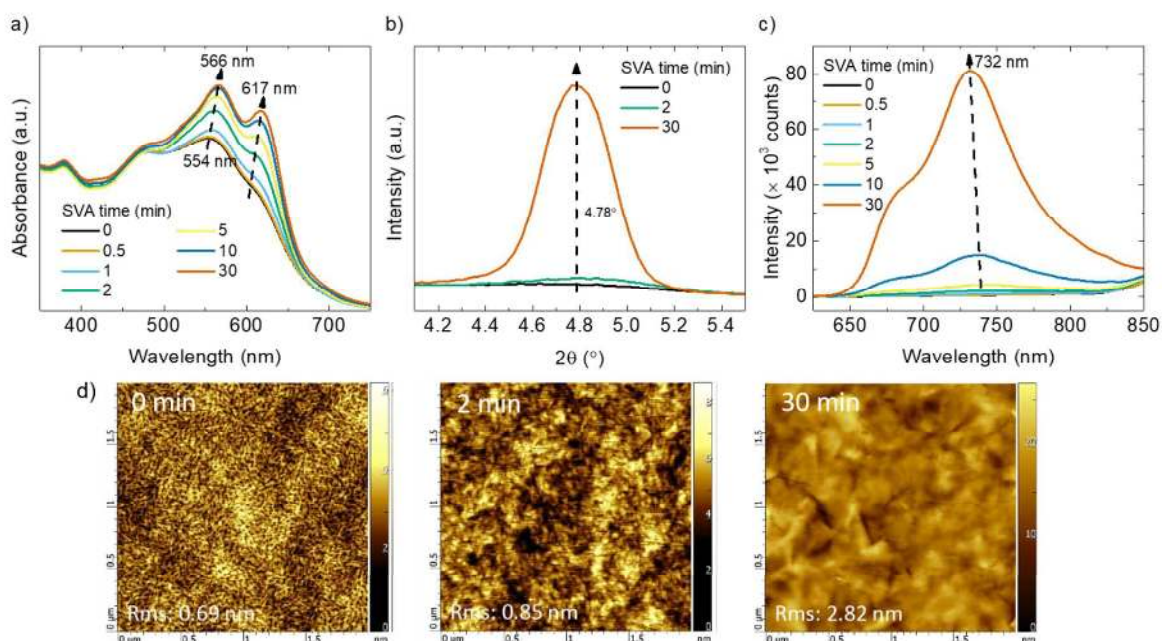
14

3.2 Effect of SVA on film morphology

Fig. 2 (a) UV-Vis absorption spectra; (b) GIXRD measurement; (c) PL spectra; and (d) AFM topographical images of the BTR:PC$_{71}$BM blend films with increasing SVA time.

To understand the effect of SVA time on the film morphology and how the morphology correlates to the device performance, UV-Vis absorption, GIXRD, PL and AFM measurements on the BTR:PC$_{71}$BM blend films were performed. Fig. 2a shows clearly that the low energy optical absorbance peaks increase in strength with increasing SVA time, along with a red shift observed for both the main peak (from 554 nm to 566 nm, whose strength increased by 31%) and the shoulder (around 617 nm) after 30 minutes SVA. This is consistent with an increase in crystallinity of the BTR phase.[18,23] This assignment is directly supported by the corresponding GIXRD data (Fig. 2b; see Fig. S4a† for a zoomed-in figure), which has a diffraction peak at $2\theta = 4.78$ (corresponding to an interlayer spacing of 1.85 nm) whose magnitude increases with increasing SVA time (an approximate 8-fold increase from

0 minutes to 30 minutes. The enhancement in absorbance and greater crystallization can explain the increase in device efficiency for devices with SVA time up to 2 minutes.

To explain the decrease in device efficiency for SVA times longer than 2 minutes, we consider the PL quenching and surface topography of the blend films with different SVA times. The PL intensity (Fig. 2c and Fig. S4c† for a zoomed-in plot) of the blend film (measuring PL from BTR) increases significantly with longer SVA times: more than 120 times larger when comparing samples with 30 minutes to 0 minutes SVA (for 0 minutes SVA, PL is too weak to be accurately measured). The PL quenching efficiencies are calculated by $1 - PL_{blend}/PL_{neat}$ for 0 minutes, 2 minutes, and 30 minutes (see Table S1†), where PL_{blend} is the maximum PL intensity of the BTR:PC$_{71}$BM blend film and PL_{neat} is the maximum PL intensity of the BTR neat film. The PL quenching is very efficient for short SVA times (> 99% for both 0 and 2 minutes SVA) but decreases to 45% for 30 minutes SVA. This indicates that long SVA times result a substantial loss of exciton separation efficiency, explaining observed the drop in J_{SC} and EQE. Note that the PL peak position is slightly blue shifted (to 732 nm for 30 minutes SVA) with longer SVA times. The much stronger PL quenching with increasing SVA time is further supported by the corresponding AFM images of the blend films, which show an increase in domain size and RMS roughness (0 minutes: 0.69 nm, 2 minutes: 0.85 nm and 30 minutes: 2.82 nm) for longer SVA times. As the domain size increases (indicating more phase separation) due to an increase in crystallization, PL is quenched less efficiently. The PL and AFM results agree well with the decrease in device efficiency when the films are over treated with SVA. Therefore, we propose that the optimum SVA time (2 minutes) represents a balance between the above two opposing effects, i.e. increase in crystallization with SVA and decrease in PL quenching for long SVA.

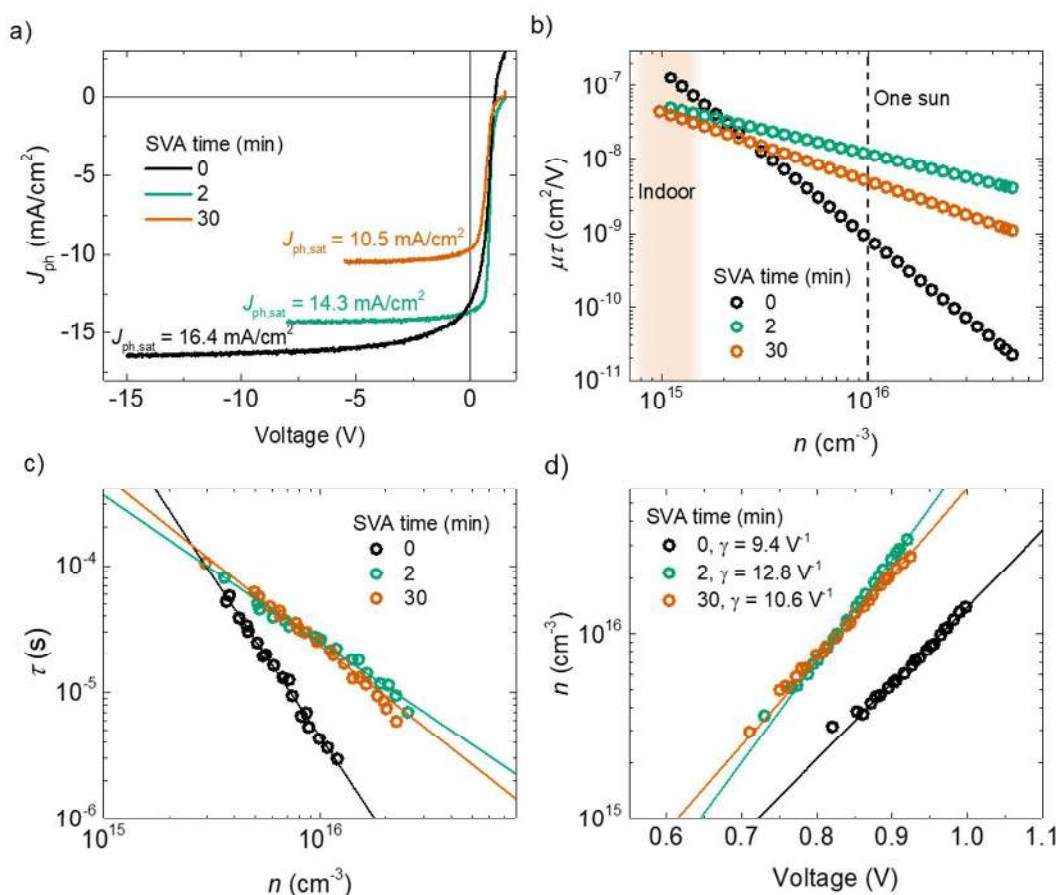## 3.3 Effect of SVA on photoelectrical properties

Fig. 3 (a) Corrected photocurrent $J_{ph} = J_{light} - J_{dark}$, the saturated J_{ph} at far reverse bias equals the total generation of current without loss. (b) Mobility lifetime product as a function of charge carrier density n, the mobility and lifetime used from the fitted data from short-circuit and open-circuit conditions respectively. (c) Charge carrier lifetime as a function of charge carrier concentration and (d) charge carrier density graph versus voltage.

To understand the effect of SVA time on device performance more quantitatively,

further optoelectronic characterization was performed to probe the dynamics of charge

generation and collection. To gain insight into the impact of SVA time on photocurrent

generation, corrected photocurrent measurements were performed in far reverse bias and

shown in Fig. 3a. By applying a large reverse bias, photo-generated charge carriers are more

efficiently extracted by the strong electric field. In principle, if the bias is high enough, all

photogenerated charge carriers can overcome recombination resulting in collection without

any loss. It can be seen that the device without any SVA process is able to generate the

highest photocurrent: in excess of 16.4 mA/cm^2, compared to 14.3 mA/cm^2 for 2 minutes

SVA and 10.5 mA/cm^2 for 30 minutes, the corresponding maximum electron-hole pair

generation rates are available in Table S2†.[30] However, J_{ph} of the 0 minutes SVA device

possesses a higher bias dependence, which is distinct from the 2 minutes and 30 minutes

cases. The large drop in J_{ph} from 2 minutes to 30 minutes correlates well with the reduced

PL quenching efficiency in Table S1†. However, for the device without SVA, the high J_{ph} at far

reverse bias is not maintained at short circuit. For all three devices, under short circuit

conditions, current loss due to non-geminate recombination appear negligible, as evidenced

by the linear behaviour of short circuit photocurrent with light intensity (see Table S2 and

Fig. S5†) and direct measurements of charge densities and recombination lifetimes as

detailed below.[31] As such, the loss of photocurrent for the 0 minutes SVA device, most likely

results from field dependent geminate recombination losses; such field dependent

recombination losses have been reported previously to be more severe in more amorphous

blends.[32]

The improved *FF* under low light implies a more efficient charge carrier collection

process. The efficiency of the charge carrier collection process is indicated by the ratio of

charge carrier drift length L_{dr} to active layer thickness: $\frac{L_{dr}}{d} = \mu\tau\frac{V_{int}}{d^2}$, here μ is the charge

carrier mobility, τ is charge carrier lifetime and V_{int} is the internal voltage within the

device.[33] The higher this ratio, the better the collection should be for a given device. The

collection efficiency of the devices under an electric field can thus be correlated with the $\mu\tau$

product. Fig. 3b shows the experimental determination of the $\mu\tau$ product over a range of

charge carrier concentration (by changing light intensity) from measurements of average

drift mobility measured from charge extraction data at short circuit (see Fig. S6†) and

charge carrier lifetime measured from transient photovoltage decays at open circuit (see Fig. 3c). Note that the 2 minutes SVA device presents the highest mobility among the three devices, ranging from 1×10^{-4} cm^2/Vs to 4×10^{-4} cm^2/Vs. Near the one sun operating condition (the charge carrier concentration at maximum power point (MPP) is around 1×10^{16} cm^{-3} for all three types of device), the $\mu\tau$ products rank 2 minutes > 30 minutes > 0 minutes, which correlates well with the *FF* under AM1.5G.

On the other hand, the charge carrier collection for devices with different SVA times under low light intensity is different from one sun. Due to much stronger negative dependence on the charge carrier density for the device without SVA, the $\mu\tau$ product is superior to that of the SVA treated devices when the charge carrier density is lower than 2×10^{15} cm^{-3} (this is around 1% sun irradiation and equivalent to indoor lighting conditions). The slopes in Fig. 3b for the three devices could be qualitatively interpreted as the difference in the improvement of the *FF* measured under AM1.5G to indoor light, the steeper the slope the more the improvement observed in *FF* (see Fig. S2†). The difference in the dependence of the $\mu\tau$ product upon light intensity is mainly governed by the increase in charge carrier lifetime with increasing charge carrier density, while the drift mobility is relatively invariant (see Fig. S6†).

Electronic energy level disorder, often observed by the presence of band edge tail (shallow trap) states can lead to differences in the dependence of carrier lifetime upon charge density.[34] The distribution of these tail states can be derived from charge carrier density versus V_{OC} measurements.[34] A typical expression of *n* as a function of *V* is $n = n_0\exp(\gamma V)$, where the constant γ quantifies the dependence of charge carrier density upon film quasi-Fermi level splitting. $\gamma \approx 19$ for ideal semiconductors, with smaller values

indicating increasingly broad distributions of tail states. Here we find that in Fig. 3d the

device with 2 minutes treatment shows the largest γ (γ = 12.8 V^{-1}) indicating the least

energetic disorder, whilst the device without treatment shows the most disordered (γ = 9.4

V^{-1}) among the three. Also, note that the γ value obtained for the 2 minutes SVA treated

BTR:PC$_{71}$BM devices is among the highest reported for bulk heterojunction OPV systems.[35–

39]

3.4 Comparison with other PV technologies and discussion of potential applications
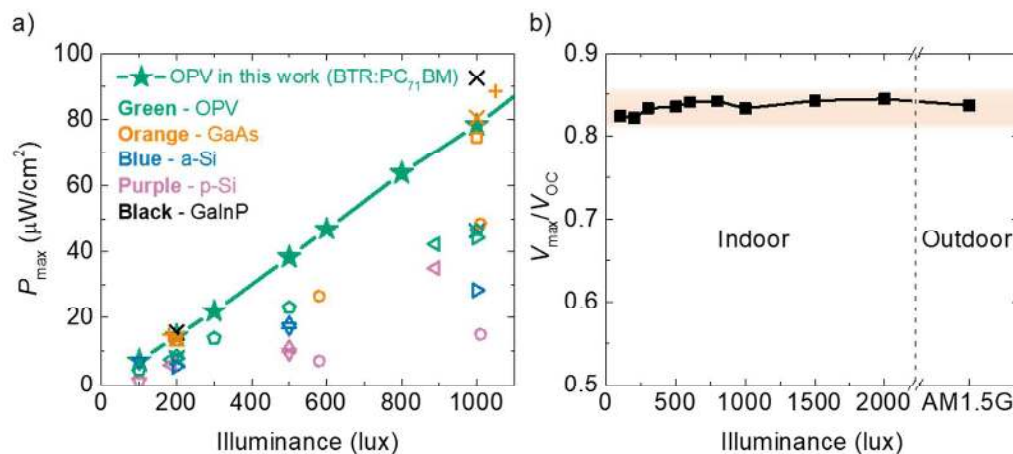

Fig. 4 (a) Maximum power density output (P_{max}) of BTR:PC$_{71}$BM device with 2 minutes SVA at different illuminance and compared to other PV techniques available in the literature. Saltire-cross symbols are from ref.[8] Cross symbols are from ref.[24] Square symbols are from ref.[10] Circle symbols are from ref.[28] Up-triangle symbols are from ref.[6] Down-triangle symbols are from ref.[9] Left-triangle symbols are from ref.[40] Right-triangle symbols are from ref.[15] Pentagon symbols are from ref.[21] (b) Ratio of V_{max} to V_{OC} of the BTR:PC$_{71}$BM device with 2 minutes SVA from indoor lighting to AM1.5G condition.

A plot of the P_{max} at different illuminance can be useful to determine the cell size needed to obtain a certain power requirement in an indoor environment in which the light level is usually fixed and stable. Fig. 4a shows the P_{max} obtained by the BTR:PC$_{71}$BM device with 2 minutes SVA at different illuminance (corresponding J-V curves are available in Fig. S7†). The plot of P_{max} against the illuminance shows nearly linear proportionality. We further compare the OPV performance with published values for inorganic PV technologies tested under indoor conditions.[6,8–10,15,21,24,28,40] Note that it may not be ideal to compare the results obtained from different research groups as the light sources could be different and there is no international standard developed for indoor PV testing.[41] Obviously, the OPV device reported here not only outperforms polycrystalline-silicon (p-Si) and amorphous-

silicon (a-Si) PV cells but also behaves comparably to gallium arsenide (GaAs) PV cells.

Moreover, our results also approach the highest indoor performance reported using gallium

indium phosphide (GaInP) as the active material.[8]

Since the absolute power generated under an indoor environment is somewhat

lower, a MPP tracking method used for outdoors may not be suitable for indoor

applications.[42] The fractional-voltage method is perhaps more appropriate for indoor

applications, which employs a pre-set voltage fraction in a circuit to track the MPP and thus

consume much less power compared to the MPP tracking method used for outdoors.[43] The

voltage fraction is defined by the ratio of the voltage at the MPP (V_{max}) to the V_{OC}, and could

vary significantly for different light levels since this ratio is closely related to the *FF*, which

changes substantially with the light intensity.[44] We have extracted this ratio for BTR:PC_{71}BM

device with 2 minutes SVA as shown in Fig. 4b. The ratio is surprisingly stable from 100 lux

to AM1.5G illumination which can be attributed to the high and stable *FF* throughout this

broad range of light levels (see Fig. S3†). Although in most typical cases PV cells may either

be used outdoors or indoors, some applications, such as PV cells integrated wearable

electronics, may require efficient function under both conditions. This result suggests that

circuit design for both indoor and outdoor use can be significantly simplified for the OPV

system studied herein.

In the real world, manufacturing larger devices is necessary. Such a device is usually

prepared by up-scalable methods and prefers an inverted device structure.[45] Inverted cells

based on the optimised active layer was fabricated as shown in Fig. S8†. Overall, the *J-V*

characteristic shows s-shape with similar J_{SC} but lower V_{OC}. We believed that these could be

due to some vertical phase segregation especially for the rather thick active layer used in

22

this system. More understanding and optimisation on the inverted device structure of this

system is needed. For up-scaling, there are some developed methods and procedures for

polymer-based PV cells. Several printing techniques such as gravure, flexographic, slot-die,

inkjet and spray coating, have been demonstrated in various types of polymer-based active

layer in organic electronics devices.[46] Thanks to the high tolerance in viscosity and solvents

for some of the techniques including slot-die, inkjet, and spray coating, the knowledge for

up-scaling the polymer-based active layer could possibly be transferred to solution-

processable small molecule:fullerene devices although they could have lower viscosity than

polymer.[46,47]

Finally, we estimate the charging time of a battery which is probably embedded in

the electronics for energy storage which could be charged by indoor PV device. Here, we

simulated a plot of charging time for three typical sizes of rechargeable battery (button, AAA,

and AA) based on our devices data under different illuminance, assuming operating in a

business card size module with consideration of practical losses. Details of the simulation

can be found in the ESI†. For example, under 1000 lux, for a button size battery, it requires

from less than one day to few days to be fully charged depending on the capacity of the

battery. Although the charging time seems long, the battery can eventually be kept fully

charged for long term operation if the power output of the indoor PV cell is higher than the

average power required for the electronics.

4. Conclusion

We have studied the performance of BTR:PC$_{71}$BM devices with SVA times ranging from 0 minutes to 30 minutes under different lighting conditions. With a moderate treatment time of 2 minutes to 5 minutes, we obtain a PCE over 10 % with up to 79 % *FF* under AM1.5G illumination and 78.2 μW/cm^2 power density generated under fluorescent lamps at 1000 lux, corresponding to a high PCE of 28.1 %, among OPV. The devices exhibit a unique stable ratio of V_{max} to V_{OC} from indoor lighting to one sun irradiation, indicating that the low power consumption fractional-voltage method is ideal for tracking the MPP over a broad range of illumination for these devices (potentially attractive for wearable PV). The effect of SVA treatment on the device performance for both AM1.5G and 1000 lux correlates well with the film morphology (a balance between enhanced crystallization and increased phase separation), and charge generation and collection dynamics, particularly the dependence of mobility-lifetime product on charge carrier density. We discover that even in the existing OPV materials, there is already highly promising material system for indoor application, which points out the importance of the selection rules utilized here. Furthermore, the advanced optoelectronic characterization techniques will be useful to understand device physics under low light levels. OPV could lead to low cost and novel indoor applications (e.g. which require flexible or/and light-weight PV) not allowed by traditional silicon PV.

Conflicts of interest

There are no conflicts to declare.

Acknowledgements

References

1   S. D. Collins, N. A. Ran, M. C. Heiber and T. Q. Nguyen, *Adv. Energy Mater.*, 2017, **7**, 1602242.

2   H. K. H. Lee, Z. Li, I. Constantinou, F. So, S. W. Tsang and S. K. So, *Adv. Energy Mater.*, 2014, **4**, 1400768.

3   D. Deng, Y. Zhang, J. Zhang, Z. Wang, L. Zhu, J. Fang, B. Xia, Z. Wang, K. Lu, W. Ma and Z. Wei, *Nat. Commun.*, 2016, **7**, 13740.

4   J. Wan, X. Xu, G. Zhang, Y. Li, K. Feng, Q. Peng, A. J. Heeger, G. C. Bazan, T. Q. Nguyen, T. Ameri, S. A. Ponomarenko, C. J. Brabec, Y. S. Chen, W. H. Steier, A. K.-Y. Jen, Y. S. Chen, Y. Cao and Y. S. Chen, *Energy Environ. Sci.*, 2017, 7992–7995.

5   N. H. Reich, W. G. J. H. M. van Sark and W. C. Turkenburg, *Renew. Energy*, 2011, **36**, 642–647.

6   Y. Li, N. J. Grabham, S. P. Beeby and M. J. Tudor, *Sol. Energy*, 2015, **111**, 21–29.

7   A. S. Teran, E. Moon, W. Lim, G. Kim, I. Lee, D. Blaauw and J. D. Phillips, *IEEE Trans. Electron Devices*, 2016, **63**, 2820–2825.

8   I. Mathews, P. J. King, F. Stafford and R. Frizzell, *IEEE J. Photovoltaics*, 2016, **6**, 230–235.

9   F. De Rossi, T. Pontecorvo and T. M. Brown, *Appl. Energy*, 2015, **156**, 413–422.

10   M. Freitag, J. Teuscher, Y. Saygili, X. Zhang, F. Giordano, P. Liska, J. Hua, S. M. Zakeeruddin, J.-E. Moser, M. Grätzel and A. Hagfeldt, *Nat Phot.*, 2017, **11**, 372–378.

11   C. Y. Chen, J. H. Chang, K. M. Chiang, H. L. Lin, S. Y. Hsiao and H. W. Lin, *Adv. Funct. Mater.*, 2015, **25**, 7064–7070.

12   F. Di Giacomo, V. Zardetto, G. Lucarelli, L. Cinà, A. Di Carlo, M. Creatore and T. M. Brown, *Nano Energy*, 2016, **30**, 460–469.

13   R. Steim, T. Ameri, P. Schilinsky, C. Waldauf, G. Dennler, M. Scharber and C. J. Brabec, *Sol. Energy Mater. Sol. Cells*, 2011, **95**, 3256–3261.

14   B. P. Lechêne, M. Cowell, A. Pierre, J. W. Evans, P. K. Wright and A. C. Arias, *Nano Energy*, 2016, **26**, 631–640.

15   Y. Aoki, *Org. Electron.*, 2017, **48**, 1123–1125.

16   C. L. Cutting, M. Bag and D. Venkataraman, *J. Mater. Chem. C*, 2016, **4**, 10367–10370.

17   M. F. Müller, M. Freunek and L. M. Reindl, *IEEE J. Photovoltaics*, 2013, **3**, 59–64.

18   K. Sun, Z. Xiao, S. Lu, W. Zajaczkowski, W. Pisula, E. Hanssen, J. M. White, R. M. Williamson, J. Subbiah, J. Ouyang, A. B. Holmes, W. W. H. Wong and D. J. Jones, *Nat. Commun.*, 2015, **6**, 6013.

19   A. Armin, J. Subbiah, M. Stolterfoht, S. Shoaee, Z. Xiao, S. Lu, D. J. Jones and P. Meredith, *Adv. Energy Mater.*, 2016, **6**, 1–10.

20   K. N. Schwarz, P. B. Geraghty, D. J. Jones, T. A. Smith and K. P. Ghiggino, *J. Phys. Chem. C*, 2016, **120**, 24002–24010.

21   H. K. H. Lee, Z. Li, J. R. Durrant and W. C. Tsoi, *Appl. Phys. Lett.*, 2016, **108**, 253301.

22   S. Yang, Z. Hsieh, M. L. Keshtov, G. D. Sharma and F. Chen, *Sol. RRL*, 2017, **1700174**, 1–6.

23   S. Engmann, H. W. Ro, A. Herzing, C. R. Snyder, L. J. Richter, P. B. Geraghty and D. J. Jones, *J. Mater. Chem. A*, 2016, **4**, 15511–15521.

24   I. Mathews, G. Kelly, P. J. King and R. Frizzell, in *2014 IEEE 40th Photovoltaic Specialist Conference*, 2014, pp. 0510–0513.

25   Indoor Dye Sensitized Solar Cells, http://gcell.com/dye-sensitized-solar-cells/advantages-of-dscc/indoor-dye-sensitize-solar-cells.

26   W. C. Tsoi, S. J. Spencer, L. Yang, a M. Ballantyne, P. G. Nicholson, a Turnbull, a G. Shard, C. E. Murphy, Bradley, J. Nelson and J. Kim, *Macromolecules*, 2011, **44**, 2944–2952.

27   K. Vandewal, A. Gadisa, W. D. Oosterbaan, S. Bertho, F. Banishoeib, I. Van Severen, L. Lutsen, T. J. Cleij, D. Vanderzande and J. V. Manca, *Adv. Funct. Mater.*, 2008, **18**, 2064–2070.

28   A. S. Teran, S. Member, J. Wong, S. Member, W. Lim, S. Member, G. Kim, Y. Lee, D. Blaauw, J. D. Phillips and S. Member, *IEEE Trans. Electron Devices*, 2015, **62**, 2170–2175.

29   S. R. Cowan, a Roy and a J. Heeger, *Phys. Rev. B*, 2010, **82**, 245207.

30   V. D. Mihailetchi, H. Xie, B. De Boer, L. J. A. Koster and P. W. M. Blom, *Adv. Funct. Mater.*, 2006, **16**, 699–708.

31   M. Stolterfoht, A. Armin, B. Philippa, R. D. White, P. L. Burn, P. Meredith, G. Juška and A. Pivrikas, *Sci. Rep.*, 2015, **5**, 9949.

32   D. Credgington, F. C. Jamieson, B. Walker, T. Q. Nguyen and J. R. Durrant, *Adv. Mater.*, 2012, **24**, 2135–2141.

33   G. F. A. Dibb, M.-A. Muth, T. Kirchartz, S. Engmann, H. Hoppe, G. Gobsch, M. Thelakkat, N. Blouin, S. Tierney, M. Carrasco-Orozco, J. R. Durrant and J. Nelson, *Sci. Rep.*, 2013, **3**, 3335.

34   T. Kirchartz and J. Nelson, *Phys. Rev. B - Condens. Matter Mater. Phys.*, 2012, **86**, 1–12.

35   A. Melianas, F. Etzold, T. J. Savenije, F. Laquai, O. Inganäs and M. Kemerink, *Nat. Commun.*, 2015, **6**, 8778.

36   F. Deledalle, T. Kirchartz, M. S. Vezie, M. Campoy-Quiles, P. S. Tuladhar, J. Nelson and J. R. Durrant, *Phys. Rev. X*, 2015, **5**, 1–13.

37   S. Wheeler, F. Deledalle, N. Tokmoldin, T. Kirchartz, J. Nelson and J. R. Durrant, *Phys. Rev. Appl.*, 2015, **4**, 29–31.

38   D. Credgington and J. R. Durrant, *J. Phys. Chem. Lett.*, 2012, **3**, 1465–1478.

39   C. G. Shuttle, B. O'Regan, A. M. Ballantyne, J. Nelson, D. D. C. Bradley, J. De Mello and J. R. Durrant, *Appl. Phys. Lett.*, 2008, **92**, 2006–2009.

40   S. Mori, T. Gotanda, Y. Nakano, M. Saito, K. Todori and M. Hosoya, *Jpn. J. Appl. Phys.*, 2015, **54**, 71602.

41   B. Minnaert and P. Veelaert, *Energies*, 2014, **7**, 1500–1516.

42   N. Femia, G. Petrone, G. Spagnuolo and M. Vitelli, *IEEE Trans. Power Electron.*, 2005, **20**, 963–973.

43   W. S. Wang, T. O'Donnell, N. Wang, M. Hayes, B. O'Flynn and C. O'Mathuna, *ACM J. Emerg. Technol. Comput. Syst.*, 2010, **6**, 1–26.

44   D. Bartesaghi, I. D. C. Pérez, J. Kniepert, S. Roland, M. Turbiez, D. Neher and L. J. A. Koster, *Nat. Commun.*, 2015, **6**, 7083.

45   I. Burgués-Ceballos, M. Stella, P. Lacharmoise and E. Martínez-Ferrero, *J. Mater. Chem. A*, 2014, **2**, 17711–17722.

46   R. R. Søndergaard, M. Hösel and F. C. Krebs, *J. Polym. Sci. Part B Polym. Phys.*, 2013, **51**, 16–34.

47   H. Kipphan, *Handbook of print media : technologies and production methods*, Springer, 2001.